Dalton Transactions

Th^{IV}–Desferrioxamine: Characterization of a Fluorescent Bacterial Probe

Journal:	*Dalton Transactions*
Manuscript ID	DT-ART-06-2021-002177.R2
Article Type:	Paper
Date Submitted by the Author:	21-Sep-2021
Complete List of Authors:	Alrich, Kelly; Los Alamos National Laboratory, Chemistry Livshits, Maksim; Los Alamos National Laboratory, Chemistry Stromberg, Loreen; Los Alamos National Laboratory, Chemistry Janicke, Michael; Los Alamos National Laboratory, Inorganic Isotope and Actinide Chemistry Nhu Lam, Mila; Los Alamos National Laboratory, Chemistry Stein, Benjamin; Los Alamos National Laboratory, Chemistry Division Wagner, Gregory; Los Alamos National Laboratory, Chemistry Abergel, Rebecca; Lawrence Berkeley National Laboratory, Chemical Sciences Mukundan, Harshini; Los Alamos National Laboratory, Kozimor, Stosh; Los Alamos Nation Laboratory, Chemistry Division Lilley, Laura M.; Los Alamos National Laboratory, Chemistry

ARTICLE

Th^{IV}–Desferrioxamine: Characterization of a Fluorescent Bacterial Probe

Received 00th January 20xx,
Accepted 00th January 20xx

DOI: 10.1039/x0xx00000x

Kelly Elise Aldrich[a†], Maksim Yuryevich Livshits[a†], Loreen Rose Stromberg[a], Michael Timothy Janicke[a], Mila Nhu Lam[a], Benjamin Stein[a], Gregory Lawerence Wagner[a], Rebecca J. Abergel[b], Harshini Mukundan[a], Stosh Anthony Kozimor[a], Laura Margaret Lilley*[a]

Diversifying our ability to guard against emerging pathogenic threats is essential for keeping pace with global health challenges, including those presented by drug-resistant bacteria. Some modern diagnostic and therapeutic innovations to address this challenge focus on targeting methods that exploit bacterial nutrient sequestration pathways, such as the desferrioxamine (DFO) siderophore used by *Staphylococcus aureus* (*S. aureus*) to sequester Fe^{III}. Building on recent studies that have shown DFO to be a versatile vehicle for chemical delivery, we show proof-of-principle that the Fe^{III} sequestration pathway can be used to deliver a potential radiotherapeutic. Our approach replaces the Fe^{III} nutrient sequestered by H_4DFO^+ with Th^{IV} and made use of a common fluorophore, FITC, which we covalently bonded to DFO to provide a combinatorial probe for simultaneous chelation paired with imaging and spectroscopy, H_3DFO_FITC. Combining insight provided from FITC-based imaging with characterization by NMR spectroscopy, we demonstrated that the fluorescent DFO_FITC conjugate retained the Th^{IV} chelation properties of native H_4DFO^+. Fluorescence microscopy with both [Th(DFO_FITC)] and [Fe(DFO_FITC)] complexes showed similar uptake by *S. aureus* and increased intercellular accumulation as compared to the FITC and unchelated H_3DFO_FITC controls. Collectively, these results demonstrate the potential for the newly developed H_3DFO_FITC conjugate to be used as a targeting vector and bacterial imaging probe for *S. aureus*. The results presented within provide a framework to expand H_4DFO^+ and H_3DFO_FITC to relevant radiotherapeutics (like ^{227}Th).

Introduction

The dawn of drug resistance among pathogenic microorganisms responsible for a variety of infectious diseases requires the development of new diagnostic and treatment strategies. One attractive strategy that has gained interest in recent years is the use of bacteria-specific siderophores, applied as targeting vectors.[1–4] Many bacterial species utilize siderophores in complex metabolic pathways, including micronutrient acquisition. For example, *Staphylococcus aureus* (*S. aureus*) - the causative agent of methicillin-resistant *S. aureus* (MRSA) infections - can utilize the siderophore desferrioxamine (H_4DFO^+, Fig. 1A) to scavenge iron from a host. In this specific case, previous studies have demonstrated that external introduction of H_4DFO^+ causes the same responses as native production.[5–8] These innate interaction mechanisms between bacteria and siderophores offer highly specific pathways by which new antimicrobial agents may be delivered directly to pathogenic cells within an infected host.[9]

Since the native role of siderophores is high-affinity metal chelation, pairing a siderophore with a radiotherapeutic metal ion offers a logical strategy to kill bacteria.[10–12] This is an extension concepts pioneered for alpha-therapeutic fungal therapies and radioimaging of bacterial infections.[13–16] Combined with the literature precedent for $M^{III/IV}$ chelation by the siderophore H_4DFO^+, and its relevance to *S. aureus* metabolism, we propose that H_4DFO^+ chelation of alpha-emitting radioisotopes presents a promising clinical target for developing bacteria-specific targeted alpha therapies.[17–20]

We are specifically interested in ^{227}Th ($t_{1/2}$ = 18.7 d, α = 6.1 MeV), and believe the potential of the proposed therapeutic $^{227}Th(HDFO)^{2+}$, warrants a re-examination of native H_4DFO^+ as a simultaneous targeting/therapeutic strategy for bacterial pathogens. Here we revisit the coordination chemistry of H_4DFO^+ with Th^{IV}, and further derivatized H_4DFO^+ with a fluorescent reporter, fluorescein isothiocyanate (FITC). This resulted in the new chelate, H_3DFO_FITC. We present this chelating fluorophore as an alternative to other reported fluorescent derivatives of DFO that suffer from solubility issues and quenching upon metal chelation, which impedes practical applications.[18,21,22] While these structures are not new to the literature, there are inconsistencies amongst previous structural assignments of H_4DFO^+ with M^{IV} species, particularly with the Pu^{IV} analogue of H_4DFO^+.[23,24] We focused on mild metalation conditions in study to be compatible with downstream radiolabeling applications in mind. Namely, pH = 5.5 at room temperature in a biologically compatible buffer (NH_4CH_3COO) routinely used for radiolabeling antibodies.

[a] Los Alamos National Laboratory, Los Alamos, New Mexico, USA 87545
[b] Department of Chemistry, University of California, Berkeley, California, 94720
† These authors contributed equally to the work presented herein.
Electronic Supplementary Information (ESI) available: [details of any supplementary information available should be included here]. See DOI: 10.1039/x0xx00000x

Fluorescent labeling of DFO serves two purposes: (1) studying both the fundamental chemistry of the chelating fluorophore (Chart 1B and D) and (2) exploring its potential as a combinatorial fluorescent and radiological probe. Towards this application, we examined the fluorescent and optical imaging properties of this probe in *S. aureus*. We propose our water-soluble H_3DFO_FITC complex will afford beneficial properties in applications with ^{227}Th toward fighting *S. aureus* infections. Results and Discussion

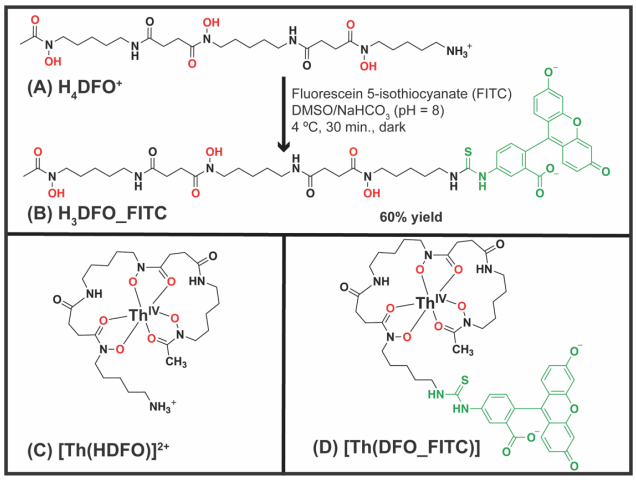

Chart 1. Reaction (*top*) and structures for the compounds under investigation with formal charges drawn at physiological pH (7.4); (A) H_4DFO^+, (B) H_3DFO_FITC, (C) $[Th(HDFO)]^{2+}$, and (D) [Th(DFO_FITC)]. Coordinating oxygens are marked in red and fluorescein is marked in green.

General Approach. With the ultimate goal of demonstrating *in vitro* labelling of *S. aureus* with our [Th(DFO_FITC)] (Figure 7), we first pursued a complete solution-state characterization of $[Th(HDFO)]^{2+}$. We deployed a suite of spectroscopic tools including NMR (1 and 2D), Raman, IR and UV-vis with Fe^{III} and $^{232}Th^{IV}$ labelled H_4DFO^+ ligand. This informed our characterization of the fluorescently labelled siderophore, H_3DFO_FITC, and the Fe^{III} and Th^{IV} labelled complexes where we deployed NMR and fluorescence spectroscopic techniques. We present a tiered approach to understand the physiochemical properties of our newly synthesized diagnostic tool. We chose to use ^{232}Th simply because we have macroscopic amounts (grams). Analogous experiments are not possible using the therapeutic ^{227}Th isotope. For reference, the amount of ^{227}Th one can safely handle in an open front hood is ~2 mCi of activity, which corresponds to ~65 pg. The macroscopic chemical characterization we present here with the ^{232}Th isotope lends credibility to future siderophore experiments with ^{227}Th.

NMR Investigation of solution structures of H_4DFO^+ and $[^{232}Th(HDFO)]^{2+}$. NMR spectra of radioactive compounds are notoriously challenging due to containment considerations. Each sample is loaded into a Teflon liner, sealed with superglue, then placed inside a secondary NMR tube that is then sealed. Teflon liners create issues for shimming and limit sample volumes. The spectra presented herein were collected under these conditions. ^{1}H NMR solution-state structural assignment for the H_4DFO^+ mesylate ($O_3SCH_3^-$ or OMs^-) salt and corresponding complex with macroscopic amounts of $^{232}Th^{IV}$, $[Th(HDFO)]^{2+}$, are presented in Figure 1. Assignments were determined from a suite of 1-D (^{1}H, ^{13}C, and DEPT-135) and 2-D NMR experiments (COSY, HSQC, HMBC) for both H_4DFO^+ OMs^- and $[Th(HDFO)]^{2+}$ (Figures S1-S11). Small quantities of impurities are present in both spectra. Metalation of H_4DFO^+ with Th^{IV} appeared to occur nearly instantaneously (before the sample can be placed in the spectrometer, ~10 min) under aqueous conditions at room temperature in D_2O with ND_4CD_3COO, pD = 5.5 (0.025 M complex). Peak shifts in the aliphatic region of the ^{1}H NMR spectrum, shown in Figure 1, are relatively subtle, on the order of ~0.1 ppm. However, given the large ionic radius of the chelated metal (Th^{IV} ionic radius = 0.972 Å) these small chemical shift differences, changes in splitting, and the appearance of new peaks (marked with a red arrow) are indicative of coordination. Broadening of the peaks is also noted in the spectrum of the Th^{IV} complex relative to the unmetalated H_4DFO^+. Analogous characterization of $[Fe(HDFO)]^+$ was not possible, owing to paramagnetic line-broadening from the Fe^{III} cation.

In previous reports, H_4DFO^+ has been observed to initially form dimers with +4 cations in solution, which then either convert to 1-to-1 complexes or remain as a dimer.[24,25] Thus, the possibility of dimer formation or alternate metal-to-ligand ratios have been suggested. This possibility with Th^{IV} was considered and diffusion ordered spectroscopy (DOSY NMR) was performed to investigate the stoichiometry of the Th^{IV} species observed by 1D and 2D NMR in solution. The DOSY experiments verified the formation of a single $[Th(HDFO)]^{2+}$ complex. Further, DOSY confirmed the chemical shifts of the OMs^- counter anion for H_4DFO^+ and the acetate (CH_3COO^-) anion associated with the solvent. Different approaches using pulsed-gradient spin echo and DOSY NMR have been employed to investigate solution phase speciation, complex stoichiometry, supramolecular complex assembly, and complicated solution interactions.[26–35] Likewise, the application of NMR derived diffusion measurements to approximate the sizes of a wide variety of molecules in solution, including

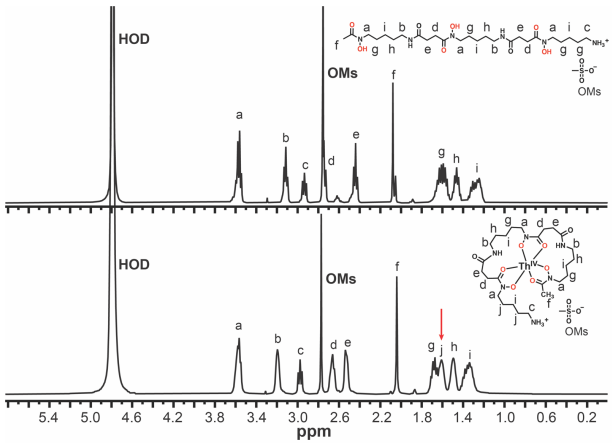

Figure 1. Solution ^{1}H NMR structures of H_4DFO^+ mesylate salt. (OMs^-, *top*) vs. $[Th(HDFO)]^{2+}$ (bottom) with a 1:1 molar ratio of Th^{IV} to DFO. The red arrow denotes a new peak that emerges upon metalation. Spectra were collected at 400 MHz, 25 °C and pD = 5.5 in ND_4CD_3COO buffer.

Table 1. Determination of diffusion coefficient and solution molecular weights of H_4DFO^+ and $[Th(HDFO)]^{2+}$ species from DOSY NMR. Internal molecular weight standards were used to calculate molecular weight. (See Supplemental Information S19-S21 for more details).

Compound	log(D) (cm^2/s)	Theoretical MW (g/mol)	Calculated log(MW) (g/mol)	Calculated MW (g/mol)
H_4DFO^+	-5.619 (± 0.008)	561.70	2.771	570 (± 76)
Th^{IV} complex (*in situ*)	-5.667 (± 0.036)	-	2.871	750 (± 88)
Potential Compound Speciation	**Predicted log(D) (cm^2/s)**	**Theoretical MW (g/mol)**		
$[Th(HDFO)]^{2+}$	-5.682	794		
$Th(HDFO)_2$	-5.808	1348		
$[Th(HDFO)]_2^{4+}$	-5.845	1580		

inorganic and organometallic chelate complexes, has become increasingly common in the last few decades.[36–43]

All of these experimental methods rely on the proportionality between the size of a molecule and the rate at which it diffuses through a solution, with smaller molecules diffusing more quickly and larger molecules diffusing more slowly, as illustrated by Equation 1 (D = diffusion coefficient, η = viscosity, r_H = hydrodynamic radius, T = temperature, k_B = Boltzmann constant).[44,45] The simplest way to approximate molecular size using DOSY NMR is to estimate the size of the studied molecule using its hydrodynamic radius (r_H). However, this method relies heavily on an accurate gradient calibration and relative consistency in a host of other experimental and fitting variables, such as convection and boundary conditions, respectively, to arrive at an accurate estimate of the unknown species' size in solution. Thus, such methods typically introduce large errors.[31] Additionally, in these cases, it is also advantageous to have an accurate model of the complex under study, *e.g.* a solid-state structure, for comparison to the observed r_H (which we lack for $[Th(HDFO)]^{2+}$). We did attempt multiple crystallization conditions including slow evaporation from aqueous media, vapor diffusion (with alcohols, ethers, and aromatics), as well as a variety of salt metastasis with non-coordinating anions.

$$D = \frac{k_B T}{6\pi\eta r_H} \quad (Eq.\ 1)$$

We chose to use a molecular-weight-derived internal calibration method to determine the size of our Th^{IV} complex *in situ,* and by association, the relative number of H_4DFO^+ ligands in each complex. The resulting DOSY spectrum provides the diffusion coefficients of the unknown, as well as the standard compounds. Using the known molecular weights (MW, g/mol) of the standard compounds in solution, a correlation between the measured log(D) (D = diffusion coefficient, cm^2/s) and log(MW) for each compound can be determined from linear regression (where m is the slope and b is the y-intercept, Equation 2). The molecular weight calibration curve can then be

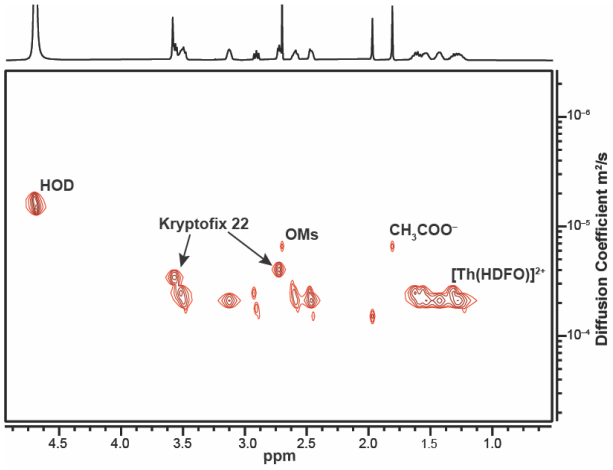

Figure 2. 2D ^{1}H-DOSY NMR of $[Th(HDFO)]^{2+}$ (~50 mM) in solution at pH 5.5 in ND_4CD_3COO buffer. A calibration curve was generated using HOD (4.70 ppm), Kryptofix® 22 (2.70 ppm, 3.52, and 3.58 ppm), and sodium acetate (CH_3COO^-, 1.90 ppm). The diffusion coefficient and molecular size of $[Th(HDFO)]^{2+}$ was determined to be 2.15×10^{-6} cm^2/s and 750 (±88) g/mol, respectively.

used to estimate the size of the unknown species in solution from its experimentally measured diffusion coefficient (D).

$$log\ (D)\ = m(log\ (MW)\ ) + b\ \ (Eq.\ 2)$$

Granted, more sophisticated treatments of the specifics of diffusion, such as temperature dependence, molecular shape differences, etc. have been examined; limitations on this method have been demonstrated, for example, when complexes of similar size but discrepant densities have been examined.[33,46] However, for the level of accuracy required to differentiate significant size differences resulting from metal-ligand complexation ratios, specifically here, monomeric vs. dimeric species ($[Th(HDFO)]^{2+}$ vs. $Th(HDFO)_2$ or $[Th(HDFO)]_2^{4+}$), this simple treatment is sufficient. Thus, a DOSY molecular weight calibration was performed for both the H_4DFO^+ (free) and $[Th(HDFO)]^{2+}$ complex, utilizing the solvent residual peak (HDO), acetate (CH_3COO^-), and Kyrptofix® 22 as internal standards. We do not account for possible coordinated waters nor CH_3COO^- a in the $[Th(HDFO)]^{2+}$, as these ligands are in fast

exchange in aqueous medium. Details on the DOSY calibration can be found on S20.

Examination of the H_4DFO^+ (Figure S16) served as a control to rule out complications in the measurement from solution ionic interactions or dramatic shape irregularities in the molecule, validating an accurate measurement.[31,47] The DOSY spectrum with $[Th(HDFO)]^{2+}$ obtained using this method is shown for illustration in Figure 2. The log(D) *vs.* log(MW) calibration curves for each sample are shown in Figure 3. Notably, we do not observe resonances that suggest that the Kryptofix® 22 has host-guest interactions with the ND_4+ buffer. The species of interest (H_4DFO^+ and $[Th(HDFO)^{2+}]$), are shown by the red and blue points where their experimental diffusion coefficients intersect the linear fit. Shown in Table 1 are the calibrated molecular weights of both species, which match the theoretical molecular weights within the error of the experiment (~12%).[47] Overall, these results suggest that the major species present in solution on the DOSY experimental time scale is a monomeric $[Th(HDFO)]^{2+}$ (1 to 1 ratio of Th^{IV} to H_4DFO^+).

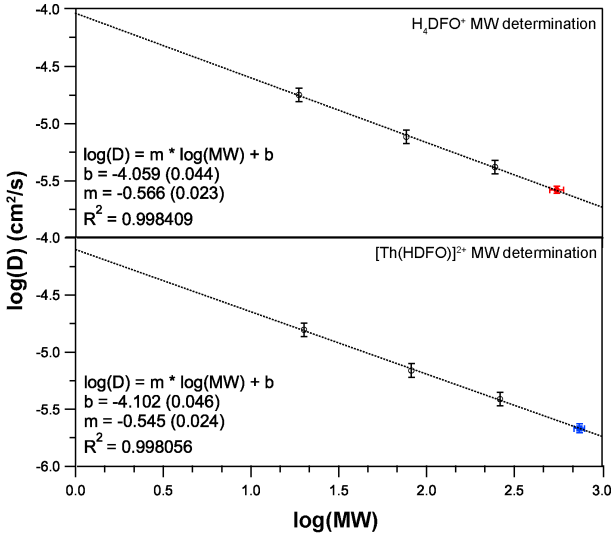

Figure 3. DOSY NMR calibration curves for H_4DFO^+ (*top*) and $[Th(HDFO)]^{2+}$ (*bottom*). Calibration curves were generated by fitting log(D) vs. log(MW) for the following standards; D_2O, Kryptofix® 22, and sodium acetate (black circles). Molecular weights of H_4DFO^+ (red circle) and $Th(HDFO)]^{2+}$ (blue square) were calculated from the linear regressions for the equation shown at the bottom left of the plots, using the experimental diffusion coefficient. Note, molecular weights were in g/mol and diffusion coefficients were in cm^2/s.

Raman and IR Spectroscopic Analysis of H_4DFO^+ and $[Th(HDFO)]^{2+}$. Vibrational spectroscopy was performed to confirm the structure of the $[Th(HDFO)]^{2+}$ complex (shown in Chart 2) and vibrational signatures further assess its potential as an IR or Raman mapping reporter. A full description of the $[Th(HDFO)]^{2+}$ structure will aid in further discussion of the Raman and IR analysis. $[Th(HDFO)]^{2+}$ can be described by three bidentate hydroxamates (red) coordinating the central Th^{IV} (purple) connected by an alternating pentyl and ethyl aliphatic backbone (blue). The linear H_4DFO^+ chelator is terminated by a methyl (black) on one of the coordinating hydroxamates and pendant aliphatic pentyl linker with a primary amine (green) protonated at physiological pH.

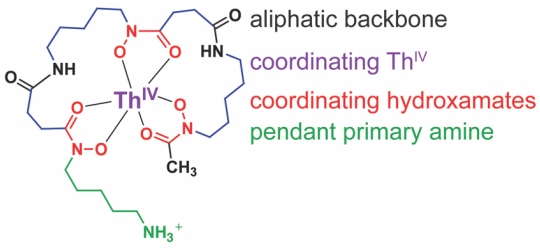

Chart 2: Coloured schematic of $[Th(HDFO)]^{2+}$ for clarity in discussing IR and Raman.

Depicted in Figure 4 are the $[Th(HDFO)]^{2+}$ Raman and infrared spectra (respectively). The $[Th(HDFO)]^{2+}$ Raman spectrum was collected at 632.8 nm (Figure 4) and 514.5 nm (Figure S31) in a 0.1 M NH_4CH_3COO, pH = 5.5, aqueous buffer solution while the infrared spectrum was collected on solid compound, deposited on a polytetrafluoroethylene IR card. The $[Th(HDFO)]^{2+}$ calculated Raman and IR spectra were generated from a single reference density functional theory optimized structure of $[Th(HDFO)]^{2+}$ (Chart 2) using ORCA 4.2.1 (see SI pages S36-S76 for details).

The solution-state Raman spectra of $[Th(HDFO)]^{2+}$ (black) and H_4DFO^+ (blue) are unsurprisingly similar. We have highlighted key shifts with grey dashed lines that give us confidence in hydroxamate binding to Th^{IV}. The following is a through description of these data. The predominant peak in the Raman spectrum of $[Th(HDFO)]^{2+}$ (Figure 4, *top*) was observed at 2939 cm^{-1} with other minor peaks found at 776, 938, 1048, 1448 and 1592 cm^{-1}. Notably, the $[Th(HDFO)]^{2+}$ Raman spectrum featured a number of broad, low intensity transitions from 750 to 1750 cm^{-1} with peaks or shoulder at 805, 1090, 1350, 1380, 1637 and 2870 cm^{-1}. Likewise, the IR spectrum of $[Th(HDFO)]^{2+}$ (Figure 4 *bottom*) revealed a number of large intensity transitions at 1042, 1159, 1315, 1590, 2846 and 2914 cm^{-1} with minor peaks at 515, 554, 720, 780, 827, 1225 and 1500 cm^{-1}. The IR spectrum also featured numerous low intensity transitions from 750 to 1750 cm^{-1}, similar to the Raman spectrum. The calculated Raman and IR spectra (Figure 4, in red) are in good agreement with the experimental data, with an intense signal at 3000 cm^{-1} and minor peaks from 450 to 1750 cm^{-1}. For reference, the H_4DFO^+ OMs^- salt in ammonium acetate buffer was also measured. The major peaks of free H_4DFO^+ are the same as the $[Th(HDFO)]^{2+}$ with the exception of the peak at 922, 1441, and 1623 cm^{-1}.

Based on our computational Raman results, we assigned the Raman and IR transitions as follows: the highest intensity transition with a maximum at 2939 cm^{-1} and the shoulder at 2870 cm^{-1} are a conglomerate of many C-H vibrational modes along with the pendent primary amine; the broad vibrations from 450 to 780 cm^{-1} are assigned to a multitude of coordinating O–C or O –Th^{IV} bond stretches and torsions; the medium intensity vibrations from 900 to 1350 cm^{-1} are assigned to the H_4DFO^+ backbone C–C bonds as well as the pendant aliphatic amine C–C bond stretches and torsion modes; lastly, the vibrations from 1420 to 1700 cm^{-1} are assigned to the coordinating O–N–C–O (hydroxamates) stretches and torsions.

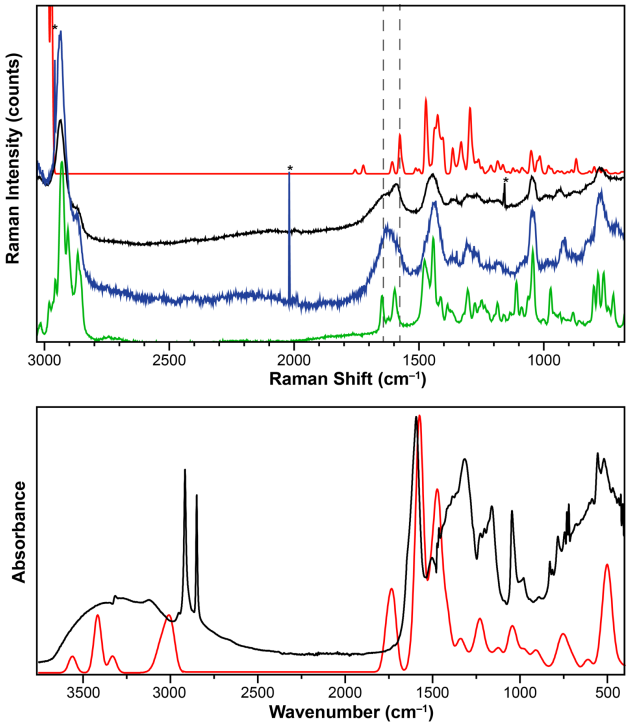

Figure 4: (*top*) 632.8 nm Raman of $[Th(HDFO)]^{2+}$ in 0.1 M NH_4CH_3COO (black) with DFT calculated Raman of $[Th(HDFO)]^{2+}$ (red). H_4DFO^+ OMs^- (green) and H_4DFO^+ in 0.1 M NH_4CH_3COO (blue) are added for comparison. Grey dashed line are indicate shifts for Th^{IV} coordination. * Raman peak resultant from a cosmic ray. (*bottom*) IR absorption of $[Th(HDFO)]^{2+}$ (black) with DFT calculated IR of $[Th(HDFO)]^{2+}$ (red).

Importantly, the splitting of the 1623 peak (free H_4DFO^+ in acetate buffer) into the peak at 1592 and shoulder at 1637 are indicative of the hydroxamates binding to Th^{IV} (Figure 4, grey dashed lines). This observation lends credibility to the DOSY NMR results that a $[Th(HDFO)]^{2+}$ complex is present in the solution. The vibrational calculations further agreed with the experimental results by predicting the observed splitting pattern of the hydroxamates as well as predicting the relative intensities of the IR and Raman features. From DFT, stronger low-frequency IR transitions are predicted from 450 to 1750 cm^{-1} as these transitions are asymmetric (more sensitive to absorption) in nature.

We do note that other signals are also observed in the vibrational spectra. The large intensity signal >3000 cm^{-1} observed in the Raman spectrum is assigned to the solvent (water) vibrations and eclipsed the higher energy N–H stretches predicted by the calculated spectrum. Likewise, the IR spectrum also featured several solvent (methanol) and polytetrafluoroethylene artifacts. It is worth noting that actinide materials cannot be dried fully due to dispersion issues. The two high-intensity peaks at 2914 and 2847 cm^{-1} are C-H stretches of polytetrafluoroethylene (from the IR card, see Methods) while the broad signals from 3000 to 3500 cm^{-1} and peaks at 550, 1038, and 1300 are residual methanol (from compound deposition solution).[48] Surprisingly, the IR and Raman activity (signal strength) at elevated concentrations is observed on the same order of magnitude relative to solvent or background electrolyte. This, in turn, decreases the likelihood that vibrational spectroscopy can be utilized as a cell mapping or metal concentration reporter when measured *in vivo*.

To gain confidence and credibility in our $[Th(HDFO)]^{2+}$ measurements, the $[Fe(HDFO)]^+$ Raman and IR spectra was also collected (Figures S30, S32, and S33). Similar to the $[Th(HDFO)]^{2+}$ treatment, vibrational calculations and prior literature precedence were used to assign the spectral features. The two predominant peaks observed in the $[Fe(HDFO)]^+$ Raman were 587 and 1580 cm^{-1}, which were consistent with previously reported surface enhanced Raman (SERS) of $[Fe(HDFO)]^+$ on silver nanoparticles.[49–51] Also consistent with the SERS of $[Fe(HDFO)]^+$ were the minor transitions at 1000, 1070, and 1210 cm^{-1}. The 587 cm^{-1} stretch was assigned to the Fe–O bond. The 1000, 1070, and 1210 cm^{-1} vibrations were assigned to the H_4DFO^+ backbone C–C stretches. The 1580 cm^{-1} peak was assigned to the O–C–N–O hydroxamate stretch. Similar to the $[Th(HDFO)]^{2+}$, the IR spectrum of $[Fe(HDFO)]^+$ also featured a number of solvent (methanol) vibrations.

Based on these data, the structural conformation of H_4DFO+ with both Fe^{III} and Th^{IV} is highly similar in solution (Raman) and the solid state (IR). The metals exhibit the same first-coordination spheres, noted by the similar O–M^{n+} and O–C–N–O bond stretches and torsions. This was further bolstered by DFT structural optimization, where we achieve similar optimized structures with Fe^{III} vs. Th^{IV}. Even with disparate charges (+1 versus +2), these structural similarities should promote similar behaviour of the compounds in solution, and in biological uptake of the siderophore-metal complexes, such as in *S. aureus*.

Synthesis of Fluorescein-tagged Desferrioxamine: DFO_FITC. Desferrioxamine was conjugated with fluorescein isothiocyanate (FITC) to study fluorescent properties in solution and in biological imaging *via* FITC fluorescence. The electrophilic carbon in the isocyanate moiety of the FITC precursor readily reacts with the nucleophilic nitrogen of the terminal primary amine under basic aqueous conditions. It is important to point out that the photosensitivity of FITC and the resultant product depicted in Scheme 1 mandate experiments be performed in the dark.

The structure of the siderophore portion of the chelate that forms binding interactions with metals was preserved (N-hydroxyamide groups), while the addition of the primary amine to the thiocyanate group generates a thiourea linkage in the conjugated product. The product, H_3DFO_FITC, was readily purified by aqueous column chromatography, using Sephadex

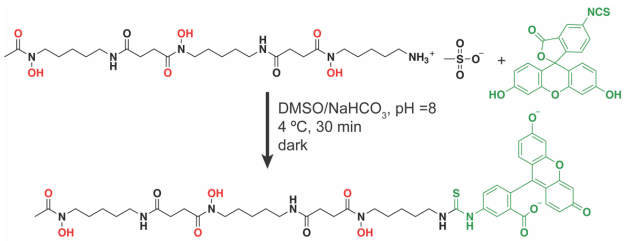

Scheme 1: Synthesis of $[H_3DFO\_FITC]$; the reaction proceeds through the nucleophilic attack of the terminal amine of H_4DFO on the isothiocyanate on FITC to generate a thiourea linker.

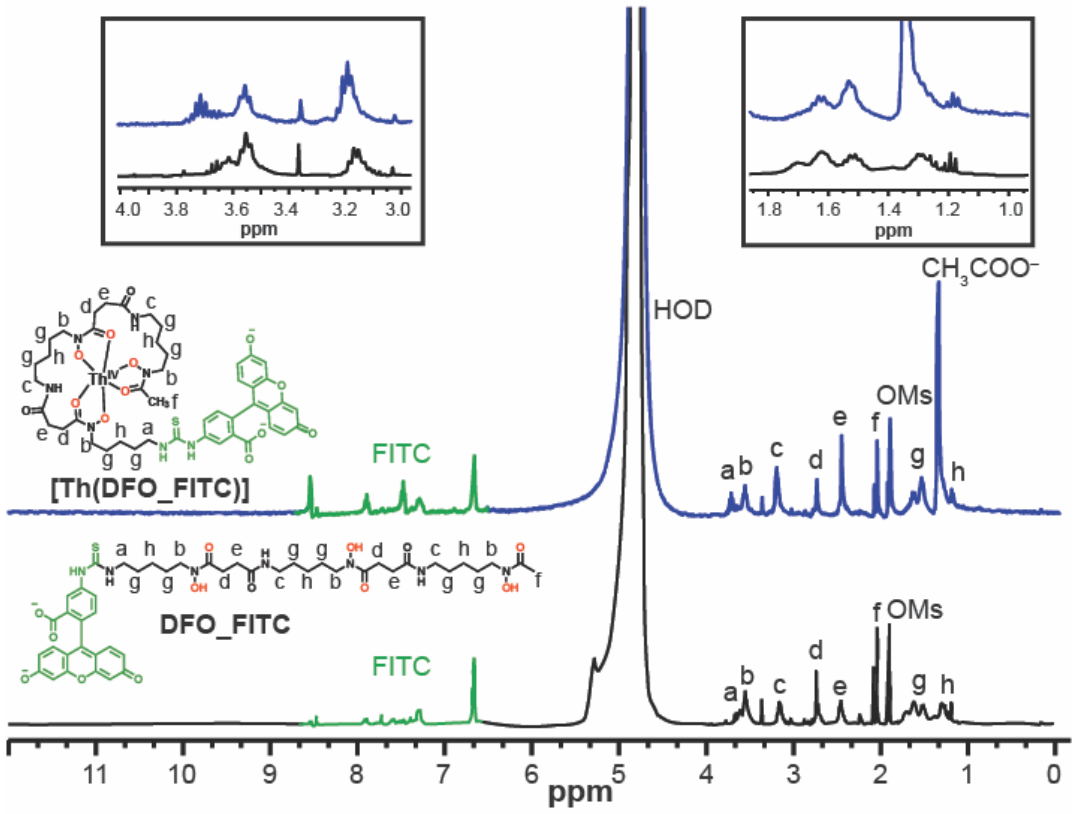

Figure 5. Solution ^{1}H NMR structures of [Th(DFO_FITC)] (*top*, blue) vs. H_3DFO_FITC (*bottom*, black) with a 1:1 molar ratio of Th^{IV} to DFO_FITC. Spectra were collected at 400 MHz, 25 °C and pD = 5.5 in ND_4CD_3COO buffer. The FITC portion of the molecule is marked in green. (*inset right and left*) The 1-1.9 ppm and 3-4 ppm regions are provided for clarity of comparison and clarity of spectral shifts upon addition of Th^{IV} .

G-10 resin as a size-exclusion stationary phase. This afforded the final fluorescence-labeled product in 60 % yield.

NMR Investigation of solution structures of H_3DFO_FITC and [Th(DFO_FITC)]. To probe the fidelity of DFO as a chelator for Th^{IV} after its functionalization with the fluorescence tag, FITC, ^{1}H NMR studies of the newly synthesized [H_3DFO_FITC] conjugate, as well as its Th^{IV} adduct [Th(DFO_FITC)], were pursued. We observed that at pD = 5.5, the solubility of [DFO_FITC] relative to H_4DFO^+ in D_2O, was reduced; this result was unsurprising given the addition of the large and hydrophobic FITC group to H_4DFO^+. The pD of the NMR solution was therefore made slightly less acidic to afford better solubility and subsequent signal-to-noise.

Unfortunately, the availability of [H_3DFO_FITC] prevented the acquisition of adequate signal-to-noise (on the 2 mg scale) for less sensitive experiments, including ^{13}C or a suite of ^{1}H-^{13}C correlation NMR experiments. However, the ^{1}H and COSY NMR data observed for $[H_3DFO\_FITC]^{2-}$ and [Th(DFO_FITC)] provided sufficient evidence of binding. The ^{1}H NMR spectra of both $[H_3DFO\_FITC]^{2-}$ and [Th(DFO_FITC)] are shown in Figure 5. This includes our assignment of the ^{1}H NMR in the non-aromatic portion of the spectrum. The most notable difference between the [H_3DFO_FITC] and H_4DFO^+ spectra was the shift in the protons adjacent to the thiourea group and the terminal ammonium group, respectively, with these protons in [H_3DFO_FITC] shifted notably more downfield.

Upon addition of Th^{IV}, similar spectral changes to those observed in Figure 1 (with H_4DFO^+) are noted here; the shifts of most peaks are slightly, but measurably altered. Additionally, the somewhat ambiguous signals attributed to the backbone methylene protons (–CH_2–) were substantially altered in their splitting and appearance (around the large peak at 1.4 ppm due to acetate in the Th^{IV} stock solution).

There was also a change in the peak shift for the “a” proton (adjacent to the FITC thiourea linkage) and a shuffling of the FITC aromatic peaks upon the addition of metal. This possibly suggests the imposition of a conformational preference for where the FITC group sits relative to the chelated Th^{IV} in the binding pocket of the chelator. Overall, the results suggest that the chelation of DFO with Th^{IV} is preserved with FITC conjugation.

Fluorescence Titrations with H_3DFO_FITC. To evaluate the [Th(DFO_FITC)] complex as a fluorescence imaging reporter, a Stern-Volmer experiment was conducted. This allowed us to probe the effects of Th^{IV} chelation on intermolecular fluorescence quenching (non-radiative excited-state deactivation). If fluorescence quenching of the FITC moiety by bound Th^{IV} was too efficient in the range of concentrations required for full complexation, the utility of the conjugate as an

imaging tool would be compromised. This was further evaluated at the equivalence of metal beyond 1:1 formation to investigate the Stern-Volmer relationship as described in Equation 3:

$$\frac{I_0}{I} = 1 + k_q\tau_0[M] \quad (Eq.\ 3)$$

Here, I_0 is the initial fluorescence intensity, I is the fluorescence intensity at a given concentration of quencher (in this case Th^{IV} or Fe^{III}), k_q is the bimolecular quenching rate constant, τ_0 is the intrinsic lifetime of the excited state, and $[M]$ is the concentration of quencher.

Depicted in Figure 6 is the [Th(DFO_FITC)] emission intensities and Stern-Volmer quenching (I_0/I) as a function of Th^{IV} concentration ($[M]$). The emission of the H_3DFO_FITC features a maximum at 521 nm with a shoulder at ~560 nm (Figure 6 *top*). Th^{IV} titration of the H_3DFO_FITC shows moderate fluorescence quenching with half of the initial intensity depleted with 5 equivalents of Th^{IV}. Further addition of Th^{IV} (past 5 equivalents) continues to decrease the emission intensity, though the exact magnitude of the quenching is difficult to measure as FITC aggregation is observed in the presence of excess cations in solution, causing the nonlinear correlation at high metal concentrations. Thus, quenching at high concentrations of Th^{IV} can't be exclusively attributed to Stern–Volmer behavior caused by intermolecular fluorescence quenching. Fitting the linear regime of the Stern-Volmer plot (up to 5 eq. of Th^{IV}) yields a bimolecular quenching rate constant of 4×10^{-9} $M^{-1}s^{-1}$ (Figure 6 *bottom*).

The origin of the [Th(DFO_FITC)] aggregation can be attributed to hydrophobic interactions between the FITC moieties, driven by increasing salt concentrations of $[Th(NO_3)_4]$. This phenomenon is well documented and can be experimentally observed by the ingrowth of scattering in the absorption spectra (see Figures S20- S21).[52] Non-linear negative deviation of Stern-Volmer relationship is also a reporter of aggregation stemming from the presence of a ground state physical barrier (aggregate material) that prevents the quencher from diffusing within the necessary range of the emitting species. Negative curvature in Stern-Volmer behavior has been observed with small molecule and polymer systems where quencher diffusion accessibility to the fluorophore changes.[53–55]

The alternate possibility that the DFO interferes with the emission quenching was ruled out using a null experiment consisting of an unconjugated fluorescein titration with Th^{IV} (Figure S26-S27), which exhibited nearly identical non-linear Stern-Volmer behavior (bimolecular quenching rate of 4×10^{-9} M^{-1} s^{-1}). With our working hypothesis that increasing salt concentration drives hydrophobic interactions between the FITC and/or fluorescein molecules, it is unsurprising there is little difference between the non-linear Stern-Volmer behavior and the shape of the emission spectra.

Again, for completeness, comparative [Fe(DFO_FITC)] Stern-Volmer quenching titrations (Figure S22-S23), as well as titration of unconjugated fluorescein with Fe^{III} (Figure S26-S27) was conducted. While the total charges between Fe^{III} and Th^{IV} are different, the fluorescence spectra and bimolecular quenching rates are similar for the iron complexes, which were calculated as 9×10^{-9} $M^{-1}s^{-1}$ and 4×10^{-9} $M^{-1}s^{-1}$, respectively. Changes in the absorption spectra best exemplify the scattering λ^4 relation, demonstrating an aggregation phenomenon (Figure S21).

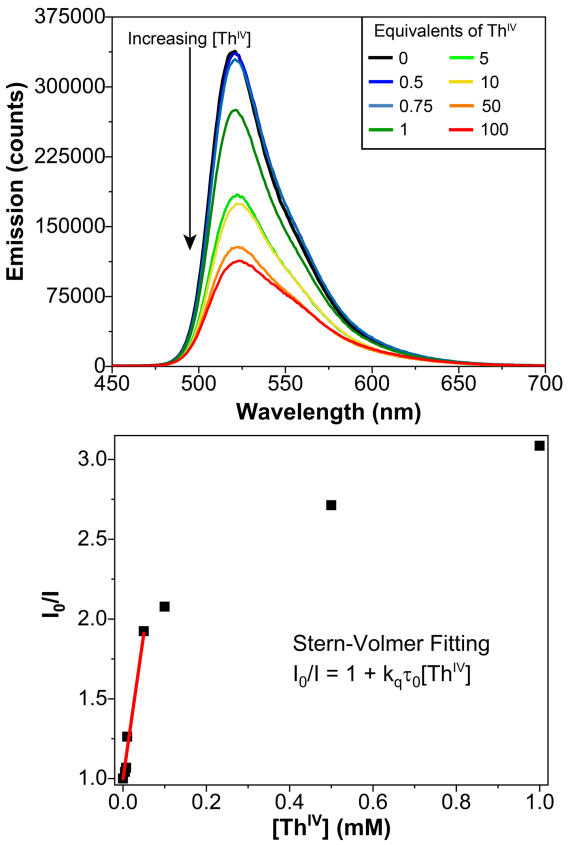

Figure 6. (*top*) H_3DFO_FITC fluorescence titration curves with Th^{IV} in equivalents of $Th(NO_3)_4$: 0 (black), 0.5 (blue), 0.75 (teal), 1 (green), 5 (lime green), 10 (yellow), 50 (orange), and 100 (red). Spectra were collected at pH 5.5 in 0.1 M NH_4CH_3COO buffer. (*bottom*) The corresponding Stern-Volmer plot of the Th^{IV} titration of H_3DFO_FITC.

These experiments provide evidence that, under the conditions relevant to 1:1 (DFO_FITC: M^{n+}) complex formation, the fluorescence intensity of the fluorophore is largely preserved, despite the introduction of intermolecular quenching pathways facilitated by metal chelation. In this 1:1 regime, the fluorescence intensity of the H_3DFO_FITC conjugate chelated with Th^{IV} or Fe^{III} is only reduced by a fraction of the fluorescence intensity from the free H_3DFO_FITC conjugate (Figure 6). Additionally, despite the linkage of the DFO and FITC portions of the conjugate through covalent bonds (*i.e.*, the thiourea group), essentially no perturbation of the λ_{max} values for absorption and emission were noted for FITC fluorescence in the chelated H_3DFO_FITC conjugate relative to unconjugated fluorescein isocyanate. These fluorescence properties will facilitate the application of existing analytical and microscopy tools developed for FITC fluorescence directly to the H_3DFO_FITC conjugate as an imaging signature.

Imaging of Staphylococcus aureus with H_3DFO_FITC. Overnight cultures of *S. aureus* were grown under full nutrient-rich conditions before treatment with either FITC (unconjugated) or

H_3DFO_FITC (uncomplexed, complexed with Fe^{III}, or complexed with Th^{IV}). Nutrient-rich conditions ensured any uptake of the [Fe(DFO_FITC)]/[Th(DFO_FITC) was not induced by micronutrient deficiency. With each treatment, a sample of 10^9 cells (CFU) were incubated with 1 µM treatment compound for one hour, washed, and mounted for microscopic imaging. Here, we demonstrate uptake and more selective fluorescent labeling of *S. aureus* with the metalated H_3DFO_FITC conjugate observed by side-by-side comparison of transmittance and fluorescence microscopy (Figure 7). In the FITC only treatment there is significant fluorescent background not observed in the treatments with the H_3DFO_FITC conjugate +/– metal. An overlay of transmittance and fluorescent images are presented in Figure S34. Biofilm production was observed (seen more clearly at higher magnification Figure S35) where we can see limited fluorescence intensity *versus* the individual cells. We can summarize that the *S. aureus* likely internalized the H_3DFO_FITC, [Fe^{III}(DFO_FITC)], [Th^{IV}(DFO_FITC)] through some active uptake mechanism.

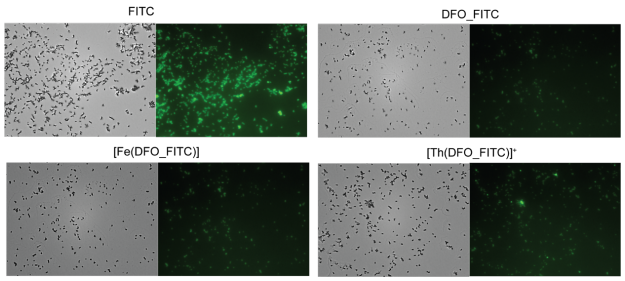

Figure 7: Transmittance and fluorescence images of *S. aureus* labelled with equal concentration of FITC, H_3DFO_FITC, [Fe(DFO_FITC)], and [Th(DFO_FITC)]. Slides were mounted in 1 x DPBS with water, then fixed. Images were acquired at 60x magnification and fluorescence was monitored at Ex: 470 nm/Em: 525 nm.

Conclusions

Here, we lay the groundwork for the important iron acquisition siderophore, H_4DFO^+, to subvert the normal iron acquisition pathways of pathogenic bacteria by incorporating the radioactive nuclide, ^{232}Th in the +4-oxidation state. We present a full solution structural characterization of DFO, and its complex with Th^{IV}. These efforts included characterization by IR/Raman measurements backed up with DFT calculations, which in turn guided our solution NMR characterization of a newly synthesized fluorescent H_3DFO_FITC reporter. We demonstrated the Stern-Volmer behavior of H_3DFO_FITC with both Fe^{III} and Th^{IV} fluorescent titrations and that fluorescent intensity is maintained as a 1 : 1 complex. Finally, we show the utility of both the Fe^{III} and Th^{IV} complexes as fluorescent imaging agents in cultures of *S. aureus*.

Characterizing the behavior of H_4DFO^+ and H_3DFO_FITC with the naturally occurring ^{232}Th isotope – which is available in macroscopic amounts and highly amenable for the presented chemical characterization – has laid a foundation for moving to medically relevant isotopes, those that cannot be handled in macroscopic quantities and whose complexation chemistry cannot be directly interrogated. Hence, current efforts are focused on using both the native $[Th^{IV}(DFO)]^{2+}$ and derivatized $[Th^{IV}$(DFO_FITC)] complexes as potential α-emitting radiotherapeutics/diagnostics, *via* the incorporation of ^{227}Th. We anticipate the bulk chemical properties of ^{232}Th will extend to the therapeutic ^{227}Th radiotherapeutic that will add to the arsenal of treatment options to combat emerging threats.

Materials and Methods

***General Considerations*:** Reagents were used without further purification; Teflon distilled water was obtained *via* distillation of MilliQ (18 MΩ) H_2O. Iron trichloride (anhydrous), thorium ICP standard (1000 ppm, 2-3 % HCl), Kryptofix® 22 (1,7,10,16-Tetraoxa-4,13,diazacyclooctadecane), desferrioxamine mesylate salt (92.5%), fluorescein isothiocyanate isomer I (>97.5 %), D_2O, CD_3COOD, ND_4OD, Sephadex G-10, tryptic soy broth, Dulbecco's Phosphate Buffered Saline (DPBS), and all acids (OPTIMA™ grade) were obtained from Sigma-Aldrich. NMR were collected on a Bruker AVANCE™ 400 MHz solution spectrometer equipped with a 5 mm broadband tunable probe for X nuclei. UV-vis spectra were collected on a Cary 6000i in a 1 mL quartz cuvette, 1 cm path length (SCC). Fluorescence spectra were collected on a Photon Technology International Spectrofluorometer QM-4/2006 in a High Precision Cell, path length 10x2 mm (Hellma Analytics) – high resolution MS was not possible for ^{232}Th labeled samples due to handling restrictions. High-resolution mass spectrometry was performed on an Agilent 6210 LC-TOF (ESI, APCI, APPI). *Staphylococcus aureus* subsp. *aureus* Rosenbach (ATCC® 25923) was purchased from ATCC. $ThCl_4 \cdot nH_2O$ was obtained as a legacy source from LANL with poorly defined origins. *Caution! ^{232}Th is a radioactive isotope that poses serious health hazards. All work with ^{232}Th was conducted in HEPA filtered fume hoods in laboratories with equipment to monitor α-, β-, and γ-radiation, by workers with training to safely handle radioactive material.*

Sample Preparation:

H_4DFO^+ NMR. H_4DFO^+ was dissolved in deuterated ammonium acetate-d_7 buffer (ND_4CD_3COO, pH = 7 in D_2O) and the pH was adjusted to 5.5 with acetic acid-d_4 (CD_3COOD) as determined by pH paper. pH paper was selected over a pH electrode due to sample handling requirements. When working with tracer amounts of material the electrode introduces contaminants and radioisotopes are known to stick to the membrane. The solution was loaded into a glass, 9 in. 400 MHz Wilmad NMR tube. ^{1}H NMR (400 MHz, D_2O): δ 3.57 (m, 6H), 3.12 (t, 4H), 2.94 (t, 2H), 2.75 (t, 4H), 2.45 (t, 4H), 2.09 (s, 3H), 1.60 (m, 6H), 1.47 (m, 4H), 1.32 (m, 2H), 1.25 (m, 4H). ^{13}C NMR (101 MHz, D_2O): δ 174.12, 173.27, 173.14, 172.88, 47.19, 46.99 (d, J = 6.9 Hz), 38.64, 38.49, 37.75, 29.74 (d, J = 12.4 Hz), 27.23, 26.91, 25.62, 24.76, 24.59, 22.36, 21.97, 18.58.

1:1 Th:H_4DFO^+ Sample: One equivalent aliquot of Th^{IV} ICP standard was dried at ambient temperature under a stream of air to avoid ThO_2 formation. H_4DFO^+ OMs^- (0.0163g, 0.0248 mmol) was dissolved in deuterated ammonium acetate-d_7 buffer (ND_4CD_3COO pH = 7 in D_2O). The H_4DFO^+ solution was added to the dried $ThCl_4$ and the pH was adjusted to 5.5 with deuterated acetic acid-d_4 (CD_3COOD) as determined by pH

paper. The reaction solution was stirred at 60 °C for 4-5 hours to ensure equilibration and complexation. The thorium sample was loaded into a Teflon liner sealed with a Teflon cap; the liner was sealed and loaded into a glass, 9 in. 400 MHz Wilmad NMR tube. ^{1}H NMR (400 MHz, D_2O): δ 3.58 (m, 6H), 3.21 (broad s, 4H), 2.99 (t, *J* = 7.6 Hz, 2H), 2.66 (broad m, 4H), 2.54 (m, 4H), 2.05 (s, 3H), 1.69 (dd, 4H), 1.63 (broad m, 4H), 1.50 (s, 4H), 1.38 (m, 6H). ^{13}C NMR (101 MHz, D_2O): δ 173.30, 165.27, 163.59, 149.76, 50.50, 49.93, 38.43, 37.34, 37.14, 29.31, 26.22, 25.27, 25.14, 24.93, 24.61, 21.41, 21.41, 16.32.

H_3DFO_FITC NMR: H_3DFO_FITC (0.001 g, 1 µmol) was dissolved in deuterated ammonium acetate-d_7 buffer (ND_4CD_3COO, pH = 7 in D_2O) and the pH was adjusted to 8 with ND_4OD as determined by pH paper. (Note: solubility was improved by raising pH) The solution was loaded into a glass, 9 in. 400 MHz Wilmad NMR tube.

[Th(DFO_FITC)] NMR: A one equivalent aliquot of Th^{IV} ICP standard was dried at ambient temperature under a stream of air to avoid ThO_2 formation. The H_3DFO_FITC solution prepared previously was added to the dried $ThCl_4$. The pH was checked (by pH paper) and was unchanged from the original pH (~8). The reaction solution was stirred at 60 °C for 4-5 h (in the dark) to ensure equilibration and complexation. The thorium sample was loaded into a Teflon liner sealed with a Teflon cap; the liner was sealed and loaded into a glass, 9 in. 400 MHz Wilmad NMR tube.

[Fe(HDFO)]$^{1+}$ Sample Preparation: H_4DFO^+ mesylate (20 mg, 30 µmol, 1 equiv.) was dissolved in deionized water and stirred at room temperature. Separately a 0.3 M stock solution of $FeCl_3$ in deionized water was prepared; 100 µL of the Fe^{III} stock solution (30 µmol, 1 equiv.) was added to the stirring solution of H_4DFO^+. Upon addition of the Fe^{III}, the clear colorless solution immediately turned an opaque dark red. The reaction was stirred for 30 min at room temperature and before the water was removed by slow evaporation to yield a dark red, glassy residue. This product was used without further purification for spectroscopic analysis.

UV-vis Titrations: $FeCl_3$ (1 mM) was prepared from the anhydrous salt dissolved in MilliQ H_2O, and thorium nitrate was prepared from an ICP stock. Spectra were collected at room temperature at pH 5.5 in NH_4CH_3COO buffer. UV-vis measurements were collected on a Varian Cary 6000i in a 1 mL quartz cuvette, data were collected in double beam mode from 800 to 300 nm.

Raman Spectroscopy: 514 and 633 nm Raman were collected on a system built in-house consisting of an argon ion gas laser (Coherent Innova 90c) or HeNe laser (Spectra Physics Model 127) as the light source, 180° light collection and a Princeton Instruments IsoPlane-320 (600 line/mm grating) with a Princeton Instruments Pixis higher performance CCD camera. The spectra for Fe^{3+} and Th^{4+} H_4DFO Raman samples were collected in 0.1 NH_4OAc buffer.

Infrared Spectroscopy: Infrared spectra were collected on a commercial ThermoFisher Scientific Nicolet ID5 ATR-FTIR. Samples were deposited on a thermo scientific disposable polytetrafluoroethylene card from methanol for ease of handling.

Fluorescence Titration: Fluorescence emission (Em) and excitation (Ex) was collected utilizing a Photon Technologies International Quanta model QM-04 fluorometer. Briefly, a 75W Xenon arc lamp is utilized as an excitation source with 1.5 mm excitation monochromator slit width. The fluorescence is collected at 90 using a R1527 red PMT with 2 mm excitation monochromator slit widths. Spectra were collected at room temperature at pH 5.5 in NH_4CH_3COO buffer.

DFT Calculations: Calculations were performed in Orca 4.2.1 to assist in the interpretation of the vibrational spectra by modeling DFO coordination around the metal center (Fe^{III} or Th^{IV}). DFT optimization was performed using the BPE Generalized Gradient Approximation (GGA) functional with the def2-SVP based set and def2/J Auxiliary basis sets for Columbic fitting for light atoms. Def2-TZVPP with def2/J and Sarc-Zora-TZVPP with Sarc/J basis sets were used for Fe and Th respectively. Once optimization convergence was reached, the final stationary point grid was enhanced to FinalGrid6. Optimized structures were checked with an analytical frequency calculation to make sure they were at a stationary point. A single point numerical frequency calculation on the optimized structure was performed with an analytical polarization component to generate the hessian file for FTIR and Raman comparison. Input files can be found in Supplemental Tables S1 and S2.

Staph aureus Growth and Treatment: *S. aureus* ATCC® 25923 was cultured from frozen glycerol stocks in sterile Tryptic Soy Broth (5 mL) incubated overnight at 37 °C shaking at 150 rpm. Cell culture density was measured by OD600 on an Eppendorf™ Biophotometer. 10^9 cells were pelleted by centrifugation at 10,000 rpm for 10 minutes in an Eppendorf MiniSpin® centrifuge. The pellets were resuspended in DPBS (1 mL) then treated with either 0.1 µM FITC, H_3DFO_FITC, [Fe(DFO_FITC)], and [Th(DFO_FITC)] incubated at 23 °C for 30 minutes. Cells were then pelleted and washed with 1 mL of DPBS three times before imaging. Transmittance and fluorescent microscopic images were acquired by fixing the cells on a glass slide then imaged with an Echo Revolve equipped with a FITC light cube Ex: 470/40 nm, Em: 525/50 nm, and Dm: 495 nm. Images were acquired at two magnifications 40x (PLAN Fluorite NA 0.75 WD 0.51mm) and 60x (PLAN Achromat Dry NA 0.80 WD 0.17 mm). Images were adjusted for brightness and contrast, then a green LUT was applied using Fiji.[56]

Synthesis of H_3DFO_FITC: In a light-protected 15 mL conical tube covered, desferrioxamine (0.007 mmol, 1 eq.) was dissolved in 1.5 mL aqueous $NaHCO_3$ buffer (100 mM, pH 8). To this solution, fluorescein isothiocyanate (FITC) (0.008 mmol, 1.1 eq), dissolved in 1600 µL of DMSO was slowly added. The reaction was mixed thoroughly, cooled, and allowed to proceed at 4 ºC for 30 min. The crude reaction mixture was then flash frozen in liquid nitrogen and the solvents were removed by lyophilization which yielded an orange, glassy residue. Sephadex G-10 (15 grams) was swollen for 24 hours in MilliQ (18 MΩ) H_2O and the crude reaction mixture was dissolved in 2.5 mL of MilliQ water and separated with a continuous flow of water. The pure material was eluted in a single orange band, frozen in liquid nitrogen, and lyophilized to an orange powder that was stored in the freezer with the exclusion of light in a yield of 60%. High-resolution mass spectrometry was performed on a Bruker Impact II q-ToF.

H_3DFO_FITC: ^{1}H NMR (400 MHz, ND_4CD_3COO, pD = 5.5 in D_2O) ^{1}H NMR (400 MHz, D_2O) δ 7.90 (m), 7.72 (s), 7.60-7.46 (m),

7.38 (d), 7.29 (d), 5.10 (s) [FITC Σ 12 H]; 3.61 (m) and 3.55 (m) (8 H); 3.16 (q, 4H); 2.72 (t, 4H); 2.46 (m, 4H)); 2.04 (s, 3H); 1.70 (s); 1.62 (s), 1.53 (m), and 1.30-1.19 (m) [Σ 19H]. HRMS calculated m/*z* = 949.39 g/mol M+H = 950.3967 g/mol, M+Na = 972.3789 g/mol, M+Na/2 = 486.6944.

[Th(DFO_FITC)]: ^{1}H NMR (400 MHz, ND_4CD_3COO, pD = 5.5 in D_2O): ^{1}H NMR (400 MHz, D_2O) δ 8.44 (d), 7.89 (m), 7.47 (m), 7.28 (3), 6.66 (m) [Σ 9 H]; 3.72 (m, *2H*); 3.56 (m, 4H); 3.19 (m, 4H); 2.73 (s, 2H); 2.45 (s, 4H); 2.04 (s, 3H); 1.63 (br/m) and 1.53 (m) [Σ 10H]; 1.29 (br/m, 8H)*; 1.10 (t, 2H). (Note: Due to the low signal to noise and shimming on a Teflon liner, a global third order Berstein Polynomial baseline correction was applied, which appeared to affect the integrations of some broad peaks. *Peak integration estimated by peak-fitting around impurities in MNova software).

Author Contributions

Aldrich, K.E.‡ and Livshits, M.Y.‡ These authors contributed equally.

Conflicts of interest

The authors declare no conflict of interest.

Acknowledgments

This research was supported by LANL LDRD-DR (20180005DR) and the U.S. Department of Energy Isotope Program, managed by the Office of Science for Nuclear Physics. BWS acknowledges the funding provided by the Director, Office of Science, Office of Basic Energy Sciences, Division of Chemical Sciences, Geosciences, and Biosciences, Heavy Element Chemistry Program of the U.S. Department of Energy (DOE). Postdoctoral support was provided in part by the Glenn T. Seaborg Institute (Aldrich). This work made use of the IMSERC at Northwestern University, which has received support from the Soft and Hybrid Nanotechnology Experimental (SHyNE) Resource (NSF ECCS-1542205), the State of Illinois, and the International Institute for Nanotechnology (IIN). The authors would particularly like to thank Saman Shafaie for his efforts in mass spectrometry. We would additionally like to thank Radiological Protection at LANL, particularly, Matthew Blane Cheatam for his continued support. We would also like to thank Kirk Rector for his dedicated support in establishing the BSL2 – Radiological Laboratory at LANL. LANL, an affirmative action/equal opportunity employer, is managed by Triad National Security, LLC, for the NNSA of the U.S. Department of Energy (contract 89233218CNA000001).

Notes and references

1 M. C. Clifton, P. B. Rupert, T. M. Hoette, K. N. Raymond, R. J. Abergel and R. K. Strong, *J. Struct. Biol. X*, 2019, **2**, 100008.

2 T. P. Tufano and K. N. Raymond, *J. Am. Chem. Soc.*, 1981, **1**, 6617–6624.

3 D. W. Whisenhunt, M. P. Neu, Z. Hou, J. Xu, D. C. Hoffman and K. N. Raymond, *Inorg. Chem.*, 1996, **35**, 4128–4136.

4 G. J. P. Deblonde, T. D. Lohrey, C. H. Booth, K. P. Carter, B. F. Parker, Å. Larsen, R. Smeets, O. B. Ryan, A. S. Cuthbertson and R. J. Abergel, *Inorg. Chem.*, 2018, **57**, 14337–14346.

5 R. J. Courcol, P. A. Lambert, P. Fournier, G. R. Martin and M. R. W. Brown, *J. Antimicrob. Chemother.*, 1991, **28**, 663–668.

6 R. J. Courcol, D. Trivier, M. C. Bissinger, G. R. Martin and M. R. W. Brown, *Infect. Immun.*, 1997, **65**, 1944–1948.

7 N. D. Hammer and E. P. Skaar, *Curr. Opin. Microbiol.*, 2012, **15**, 10–14.

8 J. H. Brock and J. Ng, *FEMS Microbiol. Lett.*, 1983, **20**, 439–442.

9 T. A. Wencewicz, U. Möllmann, T. E. Long and M. J. Miller, *BioMetals*, 2009, **22**, 633–648.

10 K. N. Raymond, in *A Paper Presented at the U.S.-Italy Workshop on Environmental Inorganic Chemistry*, 1983.

11 K. N. Raymond and W. L. Smith, in *Bonding Problems*, 1981, pp. 159–186.

12 P. W. Durbin, N. Jeung, S. J. Rodgers, P. N. Turowski, F. L. Weitl, D. L. White and K. N. Raymond, *Radiat. Prot. Dosimetry*, 1989, **26**, 351–358.

13 E. Dadachova, R. W. Howell, R. A. Bryan, A. Frenkel, J. D. Nosanchuk and A. Casadevall, *J. Nucl. Med.*, 2004, **45**, 313–320.

14 L. L. Chappell, K. A. Deal, E. Dadachova and M. W. Brechbiel, *Bioconjug. Chem.*, 2000, **11**, 510–519.

15 F. De Winter, C. Van de Wiele, F. Dumont, J. Van Durme, K. Solanki, K. Britton, G. Slegers, R. A. Dierckx and H. Thierens, *Eur. J. Nucl. Med.*, 2001, **28**, 570–574.

16 S. S. Das, D. W. Wareham, K. E. Britton, E. K. J. Pauwels, M. M. Welling, P. H. Nibbering, A. Lupetti and H. S. Balter, *J. Nucl. Med.*, 2002, 43, 1125–1127.

17 W. J. Perry, J. M. Spraggins, J. R. Sheldon, C. M. Grunenwald, D. E. Heinrichs, J. E. Cassat, E. P. Skaar and R. M. Caprioli, *Proc. Natl. Acad. Sci. U. S. A.*, 2019, **116**, 21980–21982.

18 T. A. Wencewicz, T. E. Long, U. Möllmann and M. J. Miller, *Bioconjug. Chem.*, 2013, **24**, 473–486.

19 N. P. Endicott, G. S. M. Rivera, J. Yang and T. A. Wencewicz, *ACS Cent. Sci.*, 2020, **6**, 493–506.

20 M. Petrik, E. Umlaufova, V. Raclavsky, A. Palyzova, V. Havlicek, J. Pfister, C. Mair, Z. Novy, M. Popper, M. Hajduch and C. Decristoforo, *Eur. J. Nucl. Med. Mol. Imaging*, 2021, **48**, 372–392.

21 Y. Ye, S. Bloch, B. Xu and S. Achilefu, *Bioconjug. Chem.*, 2008, **19**, 225–234.

22 L. G. Meimetis, E. Boros, J. C. Carlson, C. Ran, P. Caravan and R. Weissleder, *Bioconjug. Chem.*, 2016, **27**, 257–263.

23 M. A. Boggs, H. Mason, Y. Arai, B. A. Powell, A. B. Kersting and M. Zavarin, *Eur. J. Inorg. Chem.*, 2014, 3312–3321.

24 H. Boukhalfa, S. D. Reilly and M. P. Neu, *Inorg. Chem.*, 2007, **46**, 1018–1026.

25 N. B. Bhatt, D. N. Pandya and T. J. Wadas, *Molecules*, 2018, **23**, 638.

26 J. A. Jones, D. K. Wilkins, L. J. Smith and C. M. Dobson, *J. Biomol. NMR*, 1997, **10**, 199–203.

27 C. S. Johnson, *Prog. Nucl. Magn. Reson. Spectrosc.*, 1999,

34, 203–256.
28 C. Zuccaccia, N. G. Stahl, A. Macchioni, M. C. Chen, J. A. Roberts and T. J. Marks, *J. Am. Chem. Soc.*, 2004, **126**, 1448–1464.
29 P. S. Pregosin, P. G. Anil Kumar and I. Fernández, *Chem. Rev.*, 2005, 105, 2977–2998.
30 Y. Cohen, L. Avram and L. Frish, *Angew. Chemie Int. Ed.*, 2005, **44**, 520–554.
31 A. Macchioni, G. Ciancaleoni, C. Zuccaccia and D. Zuccaccia, *Chem. Soc. Rev.*, 2008, **37**, 479–489.
32 D. Li, I. Keresztes, R. Hopson and P. G. Williard, *Acc. Chem. Res.*, 2008, **42**, 270–280.
33 R. Neufeld and D. Stalke, *Chem. Sci.*, 2015, **6**, 3354–3364.
34 G. Pagès, V. Gilard, R. Martino and M. Malet-Martino, *Analyst*, 2017, 142, 3771–3796.
35 R. Evans, *Prog. Nucl. Magn. Reson. Spectrosc.*, 2020, 117, 33–69.
36 E. M. Lane, T. W. Chapp, R. P. Hughes, D. S. Glueck, B. C. Feland, G. M. Bernard, R. E. Wasylishen and A. L. Rheingold, *Inorg. Chem.*, 2010, **49**, 3950–3957.
37 D. Zuccaccia and A. Macchioni, *Organometallics*, 2005, **24**, 3476–3486.
38 D. Zuccaccia, S. Sabatini, G. Bellachioma, G. Cardaci, E. Clot and A. Macchioni, *Inorg. Chem.*, 2003, **42**, 5465–5467.
39 K. E. Aldrich, B. S. Billow, D. Holmes, R. D. Bemowski and A. L. Odom, *Organometallics*, 2017, **36**, 1227–1237.
40 K. E. Aldrich, D. Kansal and A. L. Odom, *Faraday Discuss.*, 2019, **220**, 208–230.
41 B. S. Billow, T. J. McDaniel and A. L. Odom, *Nat. Chem.*, 2017, **9**, 837–842.
42 M. Valentini, *Organometallics*, 2000, **19**, 2551–2555.
43 N. G. Stahl, C. Zuccaccia, T. R. Jensen and T. J. Marks, *J. Am. Chem. Soc.*, 2003, **125**, 5256–5257.
44 H. C. Chen and S. H. Chen, *J. Phys. Chem.*, 1984, **88**, 5118–5121.
45 J. T. Edward, *J. Chem. Educ.*, 1970, **47**, 261–270.
46 F. Zaccaria, C. Zuccaccia, R. Cipullo and A. Macchioni, *Chem. – A Eur. J.*, 2019, **25**, 9930–9937.
47 D. Li, G. Kagan, R. Hopson and P. G. Williard, *J. Am. Chem. Soc.*, 2009, **131**, 5627–5634.
48 I. Doroshenko, V. Pogorelov and V. Sablinskas, *Dataset Pap. Chem.*, 2013, **2013**, 1–6.
49 O. Cozar, N. Leopold, C. Jelic, V. Chiş, L. David, A. Mocanu and M. Tomoaia-Cotişel, *J. Mol. Struct.*, 2006, **788**, 1–6.
50 F. Yan, Y. K. Shrestha and C. L. Spurgeon, *Chem. Commun.*, 2013, **49**, 7962–7964.
51 G. Alberti, F. Quattrini, R. Colleoni, V. M. Nurchi and R. Biesuz, *Chem. Pap.*, 2015, **69**, 1024–1032.
52 T. Casalini, M. Salvalaglio, G. Perale, M. Masi and C. Cavallotti, *J. Phys. Chem. B*, 2011, **115**, 12896–12904.
53 T. Htun, *J. Fluoresc.*, 2004, **14**, 217–222.
54 H. S. Geethanjali, D. Nagaraja, R. M. Melavanki and R. A. Kusanur, *J. Lumin.*, 2015, **167**, 216–221.
55 J. Y. Cheon, H. M. Lee and W. H. Park, *Mar. Drugs*, 2018, **16**, 11/1-11/8.
56 J. Schindelin, I. Arganda-Carreras, E. Frise, V. Kaynig, M. Longair, T. Pietzsch, S. Preibisch, C. Rueden, S. Saalfeld, B. Schmid, J. Y. Tinevez, D. J. White, V. Hartenstein, K. Eliceiri, P. Tomancak and A. Cardona, *Nat. Methods*, 2012, **9**, 676–682.